

## 1. SUPPLEMENTARY METHODS

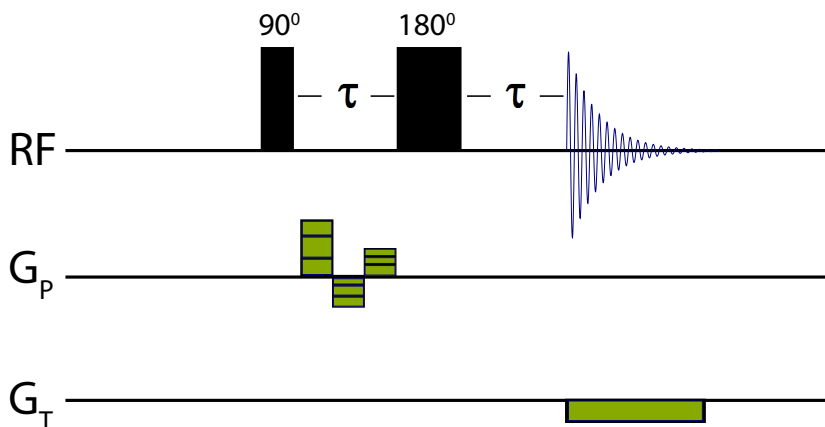


FIGURE S1. NMR pulse sequence for acquisition of thermal maps. Only a single shot (no repetition) is shown. To get a 2D image, this sequence is repeated  $n_1 \times n_2$  times while stepping the  $G_P$  gradient through the 2D phase encode scheme, where  $n_1 \times n_2$  is the number of phase encode steps.

**1.1. NMR pulse sequence.** The timing for the NMR experiment is illustrated in Figure S1. A spin echo with echo time  $2\tau$  is followed by acquisition of a free induction decay in the presence of a “temperature-encoding gradient”  $G_T$ . The temperature calibration experiment only uses the magnetic field gradient during the acquisition of the echo ( $G_T$ ). To generate images, pure phase encoding was performed using a velocity-compensated phase-encoding gradient  $G_P$ . The gradient  $G_T$  has a constant amplitude and is independent of  $G_P$ . The direction of  $G_T$  can be along  $x$ ,  $y$  or  $z$  (in which case we denote it as  $G_{T,x}$ , etc. in Section 1.7 below). The sequence is repeated for each phase-encoding step. In this study, we used a two-dimensional  $21 \times 21$  ( $n_1 \times n_2$ ) phase-encoding scheme. The  $G_P$  gradient shown stands for a two-dimensional phase encode, e.g.  $G_X$  and  $G_Y$  for an axial image or  $G_Y$  and  $G_Z$  for a coronal image. In the example shown in Fig. S1, RF pulses are hard (non-selective) pulses, the images obtained are parallel projections along the third dimension. Slice-selective pulses could also be used in different embodiments of this experiment. The delay between repetitions (“repetition time” or “recycle time”) is 3 s. The total duration of the phase-encode gradient was 3 ms and its maximum amplitude was 5 G/cm. Although not used in this study, the extension to 3D is straightforward and involves using a 3D phase encode scheme instead of a 2D scheme.

**1.2. Experimental setup.** A schematic of the investigated reactor and experimental setup is depicted in Figure S2 below. The reactor, which was placed in the RF sensitive region of the NMR instrument, contains catalyst. The reactor was operated at variable external temperatures between 293 K and 443 K. The internal temperature of the reaction often reached higher temperatures than the external temperature. For the experiments, propylene and hydrogen gases were premixed, and supplied into the reactor at constant flow rate. The tubing is coiled inside the magnet to allow thermal equilibration of the nuclear spins in the magnetic field. The gas mixture enters the reactor at the bottom of the NMR tube, flows through the catalyst-packed region, and leaves through an exhaust line at the top. This down-up flow path is required because of the RF probe design.

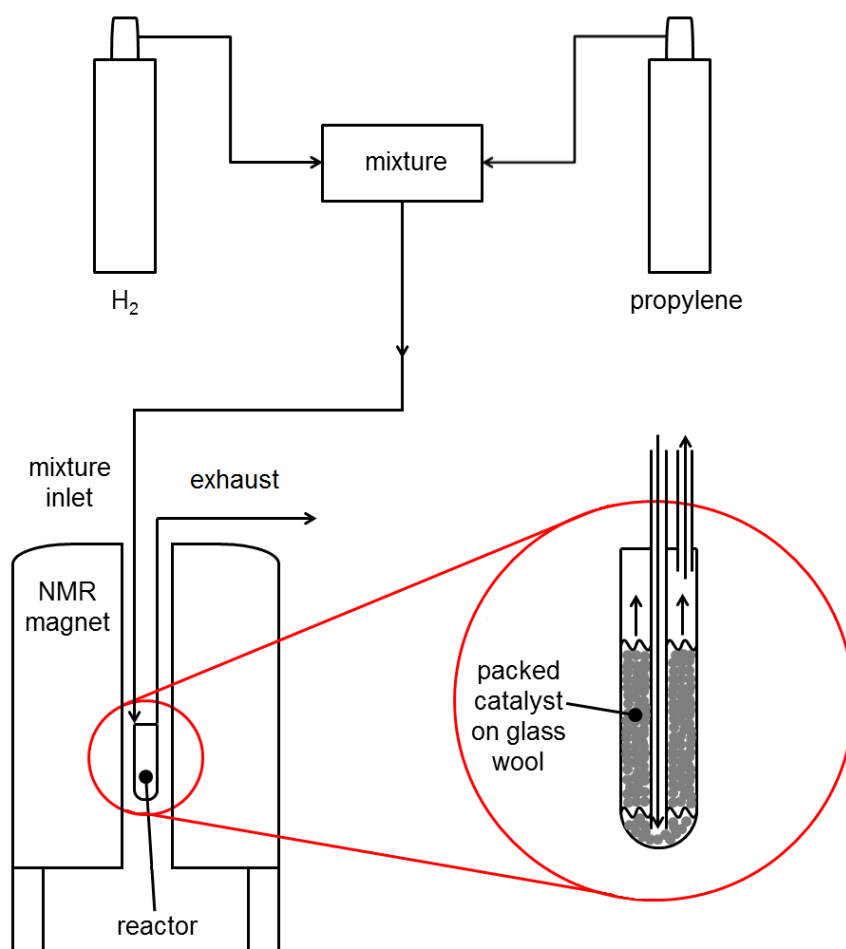


FIGURE S2. Experimental setup for acquisition of thermal maps.

**1.3. Steady conditions.** The reactor systems investigated in this Letter are operated under steady-state conditions. During the course of these experiments, the flow rate was monitored using a flowmeter and observed to remain constant within the uncertainty of the flowmeter. Figure S3 shows that the  $^1\text{H}$  NMR spectrum remains constant over a period of more than 5 hours, with constant catalytic conversion. After 5 hours, the reaction shows no sign of reduced yield.

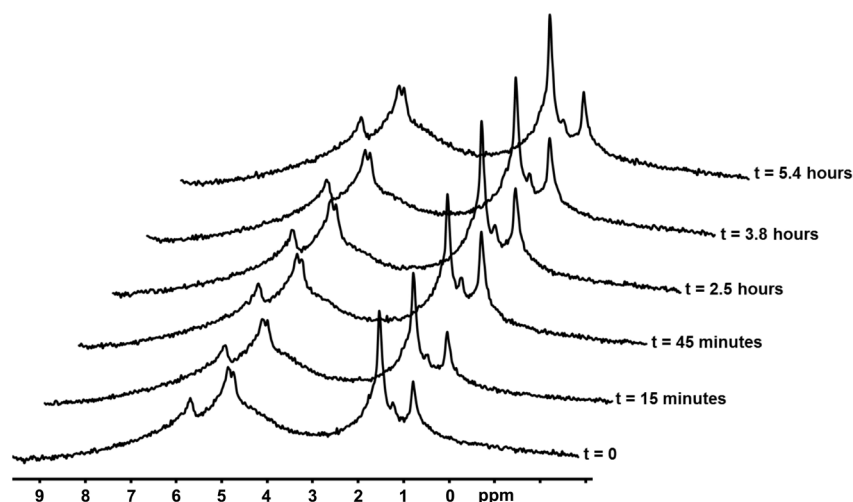


FIGURE S3. NMR spectrum of the hydrogenation reaction catalyzed by Pd-MOF in a 10 mm reactor. The reaction was monitored for several hours and exhibits a constant conversion rate over time.

The temperatures during the reaction can also be shown to be in the steady state. Figure S4 depicts thermal maps of the *in situ* hydrogenation reaction acquired immediately after catalyst activation (time = 0), after 1 hour, and after 4 hours. While spatial gradients are present (as expected), the temporal fluctuations are small. In Section 3.5.3 we discuss the effects of spatial gradients on the lineshape.

**1.4. Image voxel geometry.** Because the phase encoding scheme used in the data acquisition was two dimensional and the pulses are hard pulses (see Figure S1), the images produced in this experiment are “parallel projections”, meaning that the geometry of each voxel reflects the shape of the NMR tube. This explains, for example, why the coronal and sagittal images of Figure 3 of the main text are brighter in the center and weaker at the edges of the NMR tube. On the other hand, the signal drop-off near the top and bottom edges of the field of view is due to the drop in sensitivity of the RF coil, not because of the shape of the NMR tube. The shape of a NMR image voxel in this experiment is shown in Figure S5 below.

The RF pulse used is non-selective, which implies that the MRI images are projections across the cylindrical-shaped reactor. The NMR signal in a pixel is therefore averaged across the reactor thickness, which ranges from 0 to 8 mm when going from the reactor’s edge to its center. We note that since the NMR signal is a projection across the thickness of the

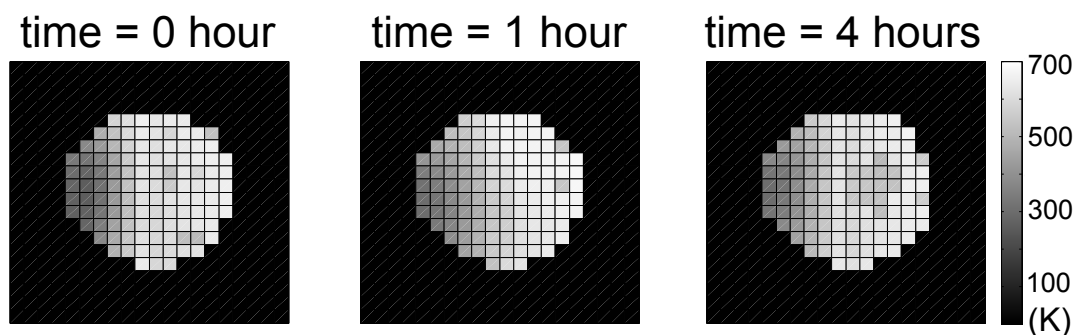


FIGURE S4. Temporal stability of thermal maps during the reaction. The hydrogenation reaction was catalyzed by Pd-MOF in a 5 mm reactor. Over the course of several hours, the reaction demonstrates constant conversion rate over time (Figure S3) as well as stable temperatures, as shown here.

reactor, temperatures cannot easily be compared between the different projections since their respective pixels represent averages performed across different directions.

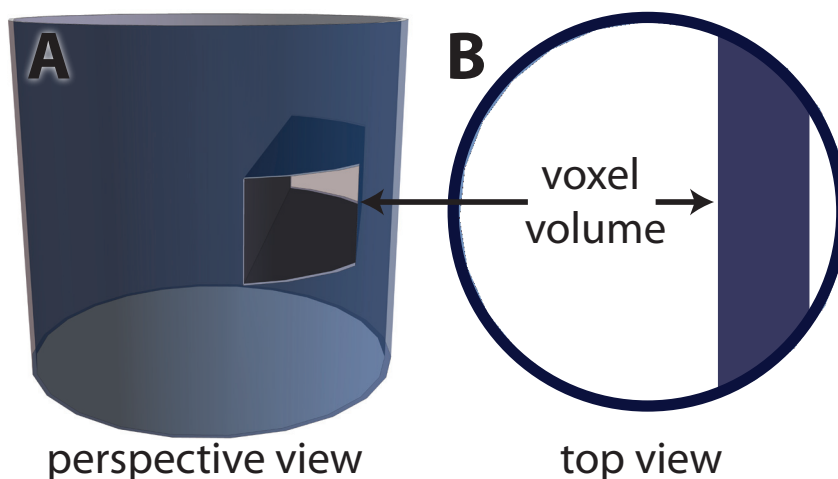


FIGURE S5. Geometry of the image voxel. (a) 3D perspective view of a voxel from a coronal or sagittal projection in relation to the NMR tube. (Only a short section of the NMR tube is shown.) (b) 2D top view. The size of the voxel relative to the NMR tube is exaggerated for illustration purposes. Roughly speaking, the shape of the gas volume giving rise to NMR signal within a voxel is that of a horizontally-aligned parallelepiped intersected with a vertical cylinder.

**1.5. Field-of-view alignment.** In order to know the position of the fiber-optic sensors in the MRI image, the field-of-view (FOV) was aligned relative to the physical coordinates

by placing water-filled glass tubes at different positions within the FOV following by the acquisition of MRI scans. The positions of the glass tubes were measured using a caliper, with precision better than 100  $\mu\text{m}$ . When dealing with coronal vs sagittal projections, we used the manufacturer-specified directions for  $x$  and  $y$ , as marked on the gradient stack, for alignment purposes. We estimate the accuracy of this alignment procedure to be better than 0.5 mm in all directions.

**1.6. Fiber-optic probe geometry.** The tip of the fiber-optic sensor has an external diameter of approximately 1 mm, which is on the order of the size of a voxel (in-plane dimension). However, along the third dimension where the voxel is projected, the ratio of the sensor volume to the voxel depth varies from point to point along the width of the NMR tube (as can be inferred from the diagram of Figure S5). When the probes are placed near the wall of the NMR tube, approximately 80% of the voxel volume is occupied by the fiber-optic sensor. When the probes are placed near the center of the tube, this ratio is approximately 40%. The NMR-derived temperature readout in our experiments is an average along the depth of each voxel.

**1.7. Effect of gradient direction.** A simple but important control experiment consists of verifying that the thermal maps are independent of the choice of gradient direction. Otherwise, any discrepancy arising from the choice of gradient direction would be a source of error in the derived temperature measurement. The control experiments were performed on a 14 T Bruker AV 600 MHz system. A 5 mm NMR tube with J Young valve was filled with 45 PSI propylene and inserted into the magnet. Axial images were acquired at 5 different temperatures (305 K, 316 K, 326 K, 337 K and 346 K) after equilibration to promote spatially uniform temperatures. In total, 441 ( $n_1 \times n_2 = 21 \times 21$ ) phase encoding steps were performed with gradients in  $x$  and  $y$  direction of 2 G/cm maximal strength ( $G_P$  gradient shown in Fig. S1). The gradient time for velocity-compensated phase-encoding was set to 3 ms and the echo time to 26 ms. At each temperature two images were recorded with either a temperature encoding gradient in  $x$ - or  $y$ -direction (0.1 G/cm) switched on during the data acquisition to introduce a line broadening ( $G_T$  gradient shown in Fig. S1). The thermal maps are shown in Figure S6 and are in good agreement at each target temperature, with variation in a single thermal map within  $\pm 2$  K. The discrepancies that result from choice of gradient direction are less than 4%. Each pixel corresponds to a region of approximately  $0.27 \times 0.27$  mm<sup>2</sup>, whereas the depth is determined by the sensitivity of the RF coil region along the  $z$  direction and is approximately 5 mm.

## 2. SUPPLEMENTARY EQUATIONS

Random molecular motion has the effect of causing nuclear spins to experience the “average field” more effectively, leading to line narrowing. Motional narrowing effects on the NMR lineshape in inhomogeneous fields were first studied by Bloembergen, Purcell and Pound [1] and later by Kubo [2]. However, the use of motional narrowing effects in an external gradient for thermometry, as is done here, is a novel concept. Here, we present a simple theoretical analysis of the observed effects.

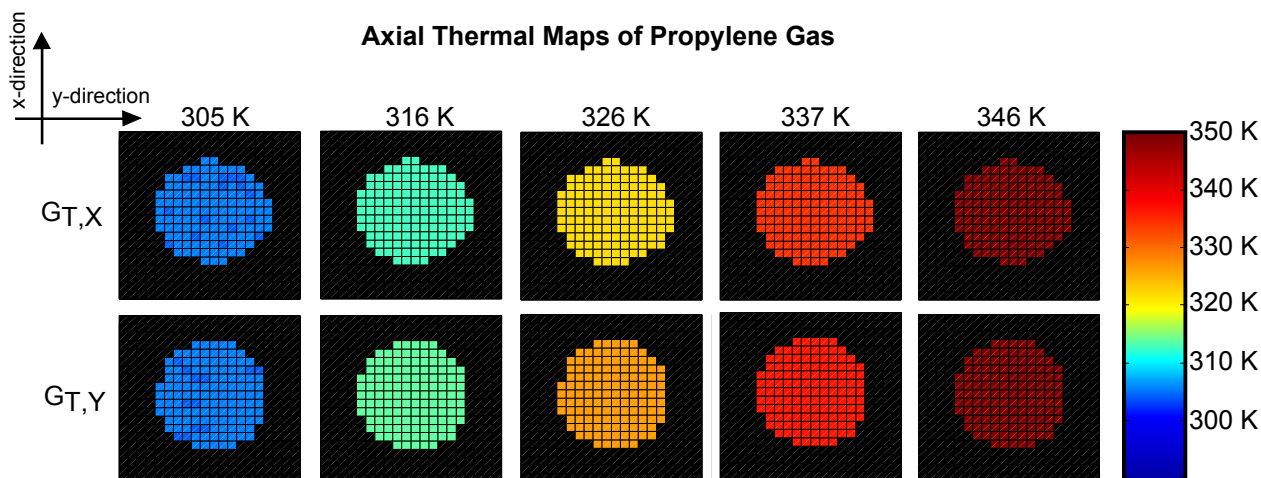


FIGURE S6. Thermal maps acquired using  $x$  versus  $y$  gradients yield similar results within 4% error. The upper row corresponds to axial images acquired with a temperature gradient along the  $x$ -direction, and the lower row corresponds to axial images acquired with a temperature gradient along the  $y$ -direction.

**2.1. Single component gases.** The first case of interest is that of a single molecular species. The NMR signal  $s(t)$  from an ensemble of spins initially located at  $x(0)$  is proportional to the expectation value [3]

$$(1) \quad \left\langle \exp \left( i \int_0^t \omega(t') dt' \right) \right\rangle = \exp \left( i \gamma_n g \int_0^t \langle x(t') \rangle dt' - \gamma_n^2 g^2 \int_0^t \langle \delta x(t') \delta x(0) \rangle (t - t') dt' \right)$$

where  $\omega(t) = \gamma_n g \cdot x(t)$  with  $g$  the applied gradient,  $\gamma_n$  is the nuclear gyromagnetic ratio and  $x(t)$  is the particle position at time  $t$ . The equality follows by assuming that  $x(t)$  is a wide-sense stationary Gaussian random process. The first term,  $i \gamma_n g \int_0^t \langle x(t') \rangle dt'$ , is oscillatory and results in a frequency shift similar to the “frequency encoding” step of MRI. Its effect is to report on the morphology of the sample. The second term describes the signal decay, and therefore, the linewidth.

**2.1.1. Position autocorrelation function.** A proper treatment of the position autocorrelation function  $\langle x(t)x(0) \rangle$  for self-diffusion of a gas molecule within a fluid of “like molecules” requires kinetic theory, which is beyond the scope of this discussion. In order to keep the present discussion simple and mathematics to a minimum, we shall instead use a Langevin description. While the latter is at best qualitative, it does capture the key elements of the observed temperature effects.

The “generalized Langevin equation (GLE) with memory kernel” is:

$$(2) \quad M\dot{v} + \int_0^t \Gamma(t-t')v(t')dt' = \eta(t),$$

where  $v(t) = \dot{x}(t)$  and  $M$  is the mass of a “Brownian” particle. By the fluctuation-dissipation theorem, the stochastic force  $\eta(t)$  describes colored noise  $\langle \eta(0)\eta(t) \rangle = kT\Gamma(t)$ .  $T$  is temperature and  $k$  is Boltzmann’s constant.

For stationary in the wide sense random process, the time-correlation function  $\langle x(t)x(0) \rangle$  can be obtained from  $\langle v(t)v(0) \rangle$  by integrating twice:

$$(3) \quad \langle v(t)v(0) \rangle = -\frac{d^2}{dt^2} \langle x(t)x(0) \rangle.$$

Projecting equation (2) with the operator  $\langle v(0), \cdot \rangle$  yields the deterministic equation:

$$(4) \quad M\langle v(0)\dot{v}(t) \rangle + \int_0^t \Gamma(t-t')\langle v(0)v(t') \rangle dt' = 0.$$

Integrating this velocity autocorrelation function once

$$(5) \quad \nu(t) = \int_0^t \langle v(0)v(t') \rangle dt',$$

and using the equipartition theorem,  $\langle v(0)v(0) \rangle = kT/M$ , as the initial condition, we get:

$$(6) \quad M\dot{\nu}(t) + \int_0^t \Gamma(t-t')\nu(t')dt' = kT.$$

The delayed response of the surrounding viscous fluid in the Ornstein-Uhlenbeck process is described by the memory kernel

$$\Gamma(t) = (\gamma^2/m) \exp(-\gamma t/m),$$

where  $\gamma$  is the friction coefficient which is proportional to the viscosity of the medium and  $m$  is the mass of molecules in the surrounding medium causing friction. Denoting  $\zeta_{-,+} = (\gamma/2m)(1 \mp \sqrt{1-4m/M})$ , the solution to equation (6) can be obtained by Laplace transformation,

$$(7) \quad \nu(t) = \frac{kT}{M} \left\{ \frac{\gamma}{m\zeta_- \zeta_+} + \frac{1}{\zeta_+ - \zeta_-} \left[ \left(1 - \frac{\gamma}{m\zeta_+}\right) e^{-\zeta_+ t} - \left(1 - \frac{\gamma}{m\zeta_-}\right) e^{-\zeta_- t} \right] \right\}.$$

From this we get the position autocorrelation function,

$$(8) \quad \langle x(t)x(0) \rangle = \frac{kT}{M(\zeta_+ - \zeta_-)} \left[ \zeta_+^{-1} \left(1 - \frac{\gamma}{m\zeta_+}\right) e^{-\zeta_+ t} - \zeta_-^{-1} \left(1 - \frac{\gamma}{m\zeta_-}\right) e^{-\zeta_- t} \right],$$

in agreement with Nørrelykke [4], who used a different method.

There are two cases of interest:  $4m = M$  is called “critically damped” and  $M > 4m$  is the overdamped case. Both cases are shown in Figure S7 below. The “underdamped” case which yields damped oscillatory solutions is discussed in Nørrelykke [5].

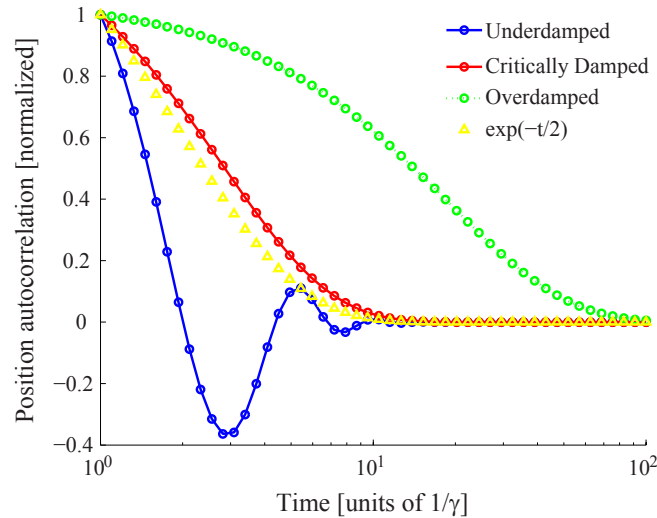


FIGURE S7. Position autocorrelations  $\langle x(t)x(0) \rangle / \langle x^2 \rangle$  for particle motion driven by viscous thermal noise in the case of overdamped, underdamped and critically damped motion. For reference, the exponential decay  $\exp(-t\gamma/2m)$  is shown ( $\gamma = 1$ ,  $m = 1$ ,  $kT = 1$ ).

The Langevin equation is valid in the limit  $m/M \rightarrow 0$ . Standard Brownian motion of large Brownian particles ( $M \gg m$ ) is strongly overdamped. See, for example, the experiment of Huang et al. (2011) [4], who used  $1 \mu\text{m}$  silica particles in water, which corresponds to a mass ratio  $M/m \sim 10^{10}$ . In our experiments we have  $m = M$ , which falls outside the range of validity of the Langevin equation. The latter thus provides at best a qualitative description of our experiment — the stochastic force is not likely to be of the correct magnitude if  $m = M$ . To ensure the validity of the Langevin model we must assume the condition  $M \gg m$  ( $m/M \rightarrow 0$ ). In Ref. [4], the Langevin model with  $M/m \sim 10^{10}$  was validated with experimental results at the single particle level.

**2.1.2. Temperature dependence of autocorrelation function.** Integrating this expression from 0 to  $t$  as required by (1), and using the approximation  $\gamma t/m \gg 1$  (observation time much longer than timescale of molecular friction), yields two terms. The first is time-independent

$$F = kT(-m\zeta_-^4\zeta_+ + m\zeta_-\zeta_+^4 - \zeta_-\gamma - \zeta_+^4\gamma)/(mM\zeta_-^4(\zeta_+ - \zeta_-)\zeta_+^4)$$

and contributes only a scaling factor  $\exp(-F)$ . The second term is time-dependent,

$$(9) \quad s(t) = \exp\left(-\gamma_n^2 g^2 \frac{kT(-m\zeta_-^2\zeta_+ - m\zeta_-\zeta_+^2 + \zeta_-^2\gamma + \zeta_-\zeta_+\gamma + \zeta_+^2\gamma)}{mM\zeta_-^3\zeta_+^3} t\right),$$

and describes an exponential decay (Lorentzian line broadening).



To analyze the temperature dependence of the linewidth a model for the viscosity of the medium is needed. The Stokes law is  $\gamma = 3\pi\eta d$ , where  $\eta$  is the shear viscosity of the medium and  $d$  is the diameter of the sphere. The Sutherland's formula describes the viscosity of a wide range of gases at temperatures between  $0 < T < 600$  K and pressures up to 3.5 MPa:

$$(10) \quad \eta = \frac{\mu_0(T_0 + C)(T/T_0)^{3/2}}{T + C} \sim \frac{T^{3/2}}{T + C},$$

where  $C$  is Sutherland's constant for the gas ( $C \approx 267$  K for propane),  $\mu_0$  is the viscosity at temperature  $T_0$ . There are two regimes of interest, low and high temperatures, which are determined by the value of  $T$  compared to the Sutherland's constant  $C$ . At low temperatures,  $\eta \sim T^{3/2}$ , whereas at high temperatures  $\eta \sim \sqrt{T}$ . For gases whose viscosity obeys the Sutherland formula, the temperature dependence follows a power law:

$$(11) \quad \Delta f \sim \begin{cases} T^{-7/2}, & T < C \\ T^{-1/2}, & T > C \end{cases}$$

in which  $\Delta f$  is the linewidth.

Figure S8 shows the temperature dependence of the line broadening for the case of several different gases. In the range 300-600 K, this curve does have some curvature in it. In this study, we chose a linear approximation to this region. Linear approximations are valid over sufficiently small temperature ranges. A polynomial model could also be used for increased accuracy over larger temperature ranges. For thermometry, the only requirement is a monotonic dependence, which is seen from Figure S8 to be the case across all temperatures and pressures of interest (the Sutherland formula is independent of pressure — with errors less than  $\sim 10\%$  up to 3.5 MPa).

**2.2. Multiple component gas mixtures.** Mixture composition enters the picture through the viscosity, which is an average of the two gas mixtures. The viscosity of a mixture comprising  $n$  components,  $\eta_m$ , is the summation of partial viscosities of each of the components [6]:

$$(12) \quad \eta_m = \sum_{i=1}^n \frac{\eta_i}{1 + \frac{1}{X_i} \sum_{j=1, j \neq i}^n X_j \phi_{ij}}, \quad \phi_{ij} = \frac{\left[1 + \left(\frac{\eta_i}{\eta_j}\right)^{1/2} \left(\frac{M_j}{M_i}\right)^{1/4}\right]^2}{\frac{4}{\sqrt{2}} \left[1 + \frac{M_i}{M_j}\right]^{1/2}},$$

where  $\eta_i$  is the viscosity of the component  $i$ ,  $X_i$  is the mole fraction of component  $i$  and  $M_i$  is the molecular weight of the  $i$ -th component at temperature and pressure of the mixture.

In the limit of low and high  $T$ , the denominators in equation (12) become independent of temperature. Thus,  $\eta_m \sim T^{3/2}$  at low temperatures ( $T < C_{min}$ ) and  $\eta_m \sim \sqrt{T}$  at high temperatures ( $T > C_{max}$ ), where  $C_{min}$  and  $C_{max}$  are the smallest and largest Sutherland constants of the mixture components, respectively. This asymptotic behavior for mixtures is identical to the case of single component gases.

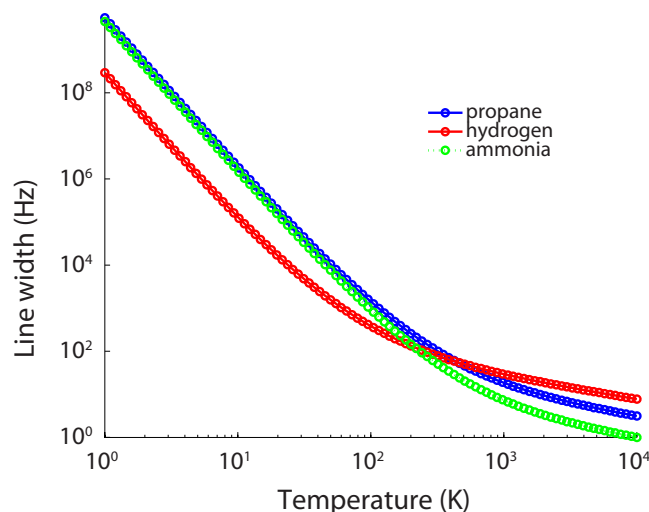


FIGURE S8. Temperature dependence of the NMR line broadening for several different values of the Sutherland constant  $C$ . The Sutherland constant separates the two temperature regions  $\Delta f \sim T^{-7/2}$  ( $T < C$ ) and  $\Delta f \sim T^{-1/2}$  ( $T > C$ ). For this calculation, we used  $M/m = 10^{10}$ ,  $g = 0.1$  G/cm and  $\gamma_n = 2\pi \cdot 42.2 \times 10^6$  rad/s/T.

In the transition region, the exponent will be a number between  $3/2$  and  $1/2$ . Thus, the temperature dependence is again monotonic, making it possible to use it as a thermometer. For example, a two-component mixture of, say, (1) propane and (2) ammonia in equal mole proportion would yield  $\eta = \frac{\eta_1}{1+\phi_{12}} + \frac{\eta_2}{1+\phi_{21}}$  together with the parameters for propane and ammonia:  $M_1=17.0$  g/mol (ammonia) and  $M_2=44.1$  g/mol (propane), the Sutherland's constant is  $C=370$  K (ammonia) and  $C=267$  K (propane). The resulting line broadening for this mixture is shown in Figure S9 and compared to that of the individual components. As can be seen, the curves are all monotonically decreasing functions of temperature and therefore enable temperature measurements with sensitivity which depends on the two components involved.

**2.3. Temperature in heterogeneous media.** Our thermometry technique is designed to measure temperature of the gas rather than that of the solid phase because NMR signal from solid materials is generally difficult to observe in this type of experiment. However, in a two-phase medium there is a (potentially) complex interaction between the gas and solid phase. In this section, we examine the effect of the solid phase on gas temperature in a heterogeneous medium. An important question is to what extent the gas phase temperature reflects that of the solid phase as a result of heat transfer processes in some “homogenized limit”.

Two examples of porous media are shown in Figure S10 below: (a) glass wool and (b) mesoporous aluminum oxide. Glass wool has very high porosity compared to many porous media, meaning that fluid molecules must travel farther to sample the temperature of solid surfaces. In our NMR experiment, the image voxel is typically much larger than the pores

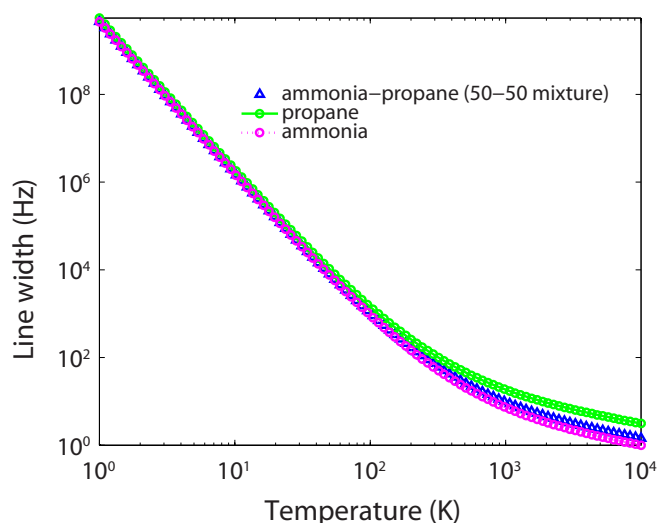


FIGURE S9. Temperature dependence of the NMR linewidth for a gas mixture (50-50) of propane and ammonia. Line broadening for the pure gases of individual components is shown for comparison. For this calculation, we used  $M/m = 10^{10}$ ,  $g = 0.1$  G/cm and  $\gamma_n = 2\pi \cdot 42.2 \times 10^6$  rad/s/T.

themselves. An example is shown by the dotted region in Figure S10(c) which comprises a mixture of pore space and solid catalyst. Thus, a proper description of the NMR experiment calls for the use of “volume-averaged” physical quantities. The catalyst medium used in this study resembles the pore space shown in Figure S10(a). Analysis of the  $\mu$ -CT images (Figure 2 of the main Letter) yielded the volume fraction of pore space in our experiments in the range of 87-89%. The volume fraction of glass wool is calculated as the ratio of the average intensity of the x-ray image in a region of interest (ROI) over the glass wool divided by the intensity of the glass wall of the NMR tube. The latter corresponds to 100% glass.

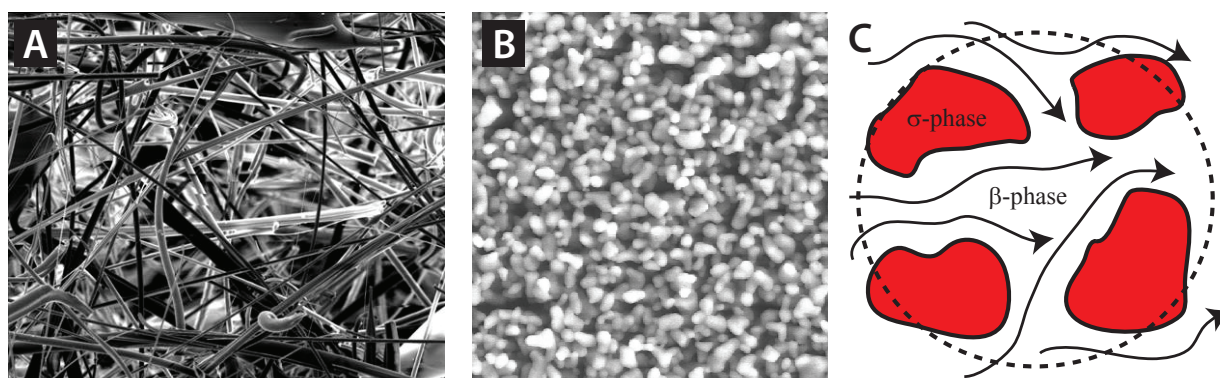


FIGURE S10. Examples of porous media. (a) Glass wool. (b) Metal nanoparticles. (c) Two-phase random medium with  $\sigma$ -phase (solid) and  $\beta$ -phase (fluid). Flow/transport is indicated by the arrows. The dotted circle denotes the averaging volume  $V$ .

In two-phase media, the heat transfer process is described in terms of the following equations and boundary conditions [7]:

$$(13) \quad (\rho c_p)_\beta \left[ \frac{\partial T_\beta}{\partial t} + \mathbf{v}_\beta \cdot \nabla T_\beta \right] = \nabla \cdot (k_\beta \nabla T_\beta) \quad \text{in } \beta\text{-phase}$$

$$(14) \quad (\rho c_p)_\sigma \frac{\partial T_\sigma}{\partial t} = \nabla \cdot (k_\sigma \nabla T_\sigma) \quad \text{in } \sigma\text{-phase}$$

$$(15) \quad T_\beta = T_\sigma \quad \text{at the } \beta - \sigma \text{ interface}$$

$$(16) \quad \mathbf{n}_{\beta\sigma} \cdot k_\beta \nabla T_\beta = \mathbf{n}_{\beta\sigma} \cdot k_\sigma \nabla T_\sigma + \Omega \quad \text{at the } \beta - \sigma \text{ interface.}$$

$\mathbf{v}_\beta$  is the velocity of the fluid in the  $\beta$  phase.  $T_i$  is the temperature of phase  $i = \beta, \sigma$ .  $\Omega$  is the thermal energy source or sink due to heterogeneous reactions at the  $\beta - \sigma$  interface.  $\mathbf{n}_{\beta\sigma}$  is the unit normal to the surface.  $k_i$  is the heat conductivity of phase  $i$ .  $(\rho c_p)_i$  is the volumetric heat capacity of phase  $i$ . These equations are of little practical use because of the presence of complex microscopic boundary conditions making the problem intractable. This is often treated with the use of effective-medium theories to upscale the partial differential equations. Two popular methods are “homogenization theory” [8] and “volume averaging” [9].

The method of volume averaging [9], for example, yields the following effective-medium description of the heat transfer process

$$(17) \quad \langle \rho \rangle C_p \frac{\partial \langle T \rangle}{\partial t} + (\rho c_p)_\beta \nabla \cdot (\phi \langle \mathbf{v}_\beta \rangle^\beta \langle T \rangle) = \nabla \cdot [(\mathbf{K}_{eff} + \mathbf{K}_D) \cdot \nabla \langle T \rangle] + (a_{\beta\sigma}/V) \langle \Omega \rangle_{\beta\sigma},$$

where  $\phi$  is the volume fraction of the fluid phase,  $A_{\beta\sigma}$  is the area per unit volume of the interface,  $\langle \Omega \rangle_{\beta\sigma}$  is the area-averaged value of  $\Omega$ ,  $\langle \rho \rangle$  represents the spatially averaged density,  $C_p$  is the mass fraction weighted heat capacity

$$(18) \quad C_p = \frac{\phi(\rho c_p)_\beta + (1 - \phi)(\rho c_p)_\sigma}{\langle \rho \rangle}.$$

$\langle T \rangle$  represents the spatially averaged temperature:

$$(19) \quad \langle T \rangle = \frac{1}{V} \int_V T dV = \phi \langle T_\beta \rangle^\beta + (1 - \phi) \langle T_\sigma \rangle^\sigma$$

with

$$(20) \quad \langle T_\beta \rangle = \frac{1}{V} \int_{V_\beta} T_\beta dV, \quad \text{and} \quad \langle T_\beta \rangle^\beta = \frac{1}{V_\beta} \int_{V_\beta} T_\beta dV = \phi^{-1} \langle T_\beta \rangle.$$

$\langle T_\beta \rangle^\beta$  is called the phase-averaged temperature.  $\mathbf{K}_{eff}$  is the effective thermal conductivity tensor defined by

$$(21) \quad \mathbf{K}_{eff} \cdot \nabla \langle T \rangle = [\phi k_\beta + (1 - \phi) k_\sigma] \nabla \langle T \rangle + \frac{k_\beta}{V} \int_{A_{\beta\sigma}} \mathbf{n}_{\beta\sigma} \tilde{T}_\beta dA + \frac{k_\sigma}{V} \int_{A_{\beta\sigma}} \mathbf{n}_{\beta\sigma} \tilde{T}_\sigma dA$$

and  $\mathbf{K}_D$  is the thermal dispersion tensor

$$(22) \quad \mathbf{K}_D \cdot \nabla \langle T \rangle = -(\rho c_p)_\beta \langle \tilde{\mathbf{v}}_\beta \hat{T}_\beta \rangle,$$

where

$$(23) \quad \langle T_\beta \rangle^\beta = \langle T \rangle + \hat{T}_\beta, \quad \mathbf{v} = \langle \mathbf{v}_\beta \rangle^\beta + \tilde{\mathbf{v}}_\beta, \quad \text{and} \quad T_\beta = \langle T_\beta \rangle^\beta + \tilde{T}_\beta.$$

This model yields a reasonable description of heat transport in a packed bed catalytic reactor. It relies on the assumption of “local thermal equilibrium” [7]. The conditions for validity of the model in relation to the physical length scales are discussed by Whitaker [7]. For steady-state flows, equation (17) describes a unique temperature  $\langle T \rangle = \langle T_\beta \rangle^\beta = \langle T_\sigma \rangle^\sigma$  whose value is determined by convective, dispersive and diffusive transport relative to the heterogeneous reaction rate at the surface.

In cases where the condition of local thermal equilibrium is not satisfied, a set of two coupled partial differential equations (see Quintard and Whitaker, Ref. [10]) describes the behavior of the two phase-averaged temperatures  $\langle T_\beta \rangle^\beta$  and  $\langle T_\sigma \rangle^\sigma$ . Only  $\langle T_\beta \rangle^\beta$  is reported directly in the NMR experiment. The degree to which the fluid phase temperature,  $\langle T_\beta \rangle^\beta$ , reflects the value of the solid phase temperature,  $\langle T_\sigma \rangle^\sigma$  is determined from equations (7.29) and (7.30) of Ref. [10] and the conductive cross-coefficients.

### 3. SUPPLEMENTARY DATA

**3.1. Effects of reaction rate.** Another possible mechanism for temperature-dependent line broadening is the timescale of the chemical reaction. If the reaction proceeds rapidly, the short lifetime of a chemical species may lead to temperature-dependent broadening because the rates of chemical reactions generally follow an Arrhenius-type law. If the NMR resonance of one of the reactants is used to measure temperature, this resonance may undergo “lifetime-broadening” as the reactants are converted into products.

Here, we show that for the reaction studied in this work, reaction rates do not lead to significant broadening. This can be done by estimating the average time scale of the chemical reaction  $aA + bB \rightarrow cC$  in the presence of transport using the advection-diffusion equation (conservation of mass species):

$$(24) \quad \rho \partial_t y_j + \rho \mathbf{v} \cdot \nabla y_j + \text{div} \mathcal{F}_j = m_j \dot{\omega}_j,$$

where  $\rho$  is the gas density,  $m_j$  is the molar mass of species  $j$ ,  $\mathbf{v}$  is the velocity,  $y_j = m_j [J] / \rho$ , and  $\mathcal{F}_j = -\rho D_j \nabla y_j$ .  $D_j$  is the diffusion constant of species  $j$ , and  $[J]$  is the concentration of species  $j$ . In the case of first-order rate reactions,  $-\dot{\omega}_A = -\dot{\omega}_B = \dot{\omega}_C = k[A][B]$ , where  $k$  is the rate constant of the reaction. For steady flows,  $\partial_t y_j = 0$ . Setting  $j = C$  yields one such equation

$$(25) \quad k[A][B] = v \cdot \nabla[C] - D_C \nabla^2[C],$$

where  $\nabla^2[C]$  denotes the Laplacian of the concentration field  $[C]$ . The time scale of the reaction is  $k[B]$ . Estimates of this quantity can be obtained from a concentration map of the species of interest, such as the one shown in Figure S11, which was extracted from the NMR data set and normalized using knowledge of the gas mixture composition and measured pressures at the inlet. With this normalization, the area under the curves of spatially-resolved NMR spectra during the reaction then provides a map of concentrations.

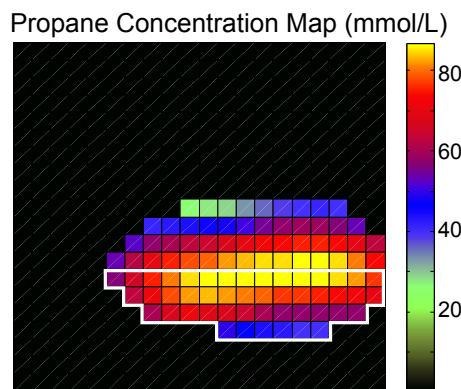


FIGURE S11. Concentration map of propane (reaction product) in the YZ plane of the catalytic reactor using MOF catalyst. Together with knowledge of the flow velocity, this map yields convective and diffusive transport contributions to the conservation of mass species, from which we obtain the reaction rates. The reaction rates are averaged in a region of interest (ROI) over the heterogeneous medium (example ROI shown in white) to yield the average timescale of the reaction.

The gradient and Laplacian were computed by finite differences using the built-in MATLAB commands `gradient` and `del2`, respectively. The step size in computing the gradient and the Laplacian of the concentration field was 0.73 mm, which is both the width and height of a single voxel. Using the average flow speed in the reactor as measured by a flowmeter placed in the flow line ( $\bar{v} = 0.75$  m/s), the average reaction time constant is found to be  $(1.4 \pm 0.2)$  Hz.

Thus, line broadening due to the chemical reaction is less than 2 Hz in our experiments, and is therefore negligible compared to the intrinsic linewidth of the gas substances in the absence of a reaction. We note that different reactions and transport conditions may lead to different outcomes.

There are at least two ways to circumvent rate-induced broadening:

- (1) by applying a stronger gradient,
- (2) by monitoring the resonance from product molecules instead of a reactant.

In the second case, product molecules are stable and their resonances do not undergo lifetime broadening.

In the event that a reactant molecule (as opposed to a product molecule) must be used for thermometry and stronger gradients are not possible<sup>1</sup>, accurate thermal maps in the presence of rate-induced broadening may still be possible if the reactor is sufficiently homogeneous and the overall temperature dependence of the linewidth is monotonic.

**3.2. Temperature coefficients of single component gases.** Here, the main properties of gas-phase thermometry in a single component gas are investigated using propylene gas by performing temperature calibration experiments at 1.0 atm for seven different gradient strengths. As gradient strength is increased, the linewidth dependence on temperature increases. The results are summarized in Table S1.

The experimental errors in Table S1 were determined from repeated measurements at each gradient strength on newly prepared samples. We note that these error bars (less than 11%) are different from reactor to reactor; this error is unrelated to the 4% error bar quoted in the main Letter, which is the uncertainty of localized temperature measurements performed within the same reactor.

Applied gradient strength (mG/cm)	Temperature coefficient (Hz/K)
0.0	$-0.01 \pm 0.01$
2.7	$-0.11 \pm 0.01$
5.3	$-0.12 \pm 0.01$
10.6	$-0.18 \pm 0.02$
15.9	$-0.20 \pm 0.01$
21.2	$-0.26 \pm 0.01$
26.5	$-0.28 \pm 0.03$

TABLE S1. Temperature coefficients for propylene at different applied gradient strengths. Pressure is 1.0 atm.

Many catalytic processes operate at high temperatures and high pressures. While the temperatures sampled in our thermal maps exceed 600 K, the method should also work at higher temperatures, as discussed in Section 2. Operation at higher pressures should also be possible based on the same theoretical arguments. Here, we show that the method works at higher pressures, and is independent of pressure up to 5 atm (as high as was allowed by our J Young valve tubes).

Temperature calibration curves were obtained for propylene gas at two additional pressures: 3.1 and 5.1 atm. For three different applied gradient strengths, the temperature coefficients were similar within experimental error (Table S7). At zero applied gradient, linewidth dependence on temperature was negligible. For nonzero applied gradients, the temperature coefficient increased with increasing gradient strength. In all cases, the results are independent of pressure within  $\pm 11\%$  of each other and exhibit no clear trends. The residual differences are likely due to different shimming conditions between experiments.

<sup>1</sup>While gradient amplitudes used in this experiment are rather modest and not limited by the available hardware, sufficiently strong gradients will eventually lead to overlap of the spectral lines and, ultimately, to the complete loss of signal.



Temperature coefficient (Hz/K) at different applied gradient strengths			
Pressure (atm)	0.0 mG/cm	5.3 mG/cm	26.5 mG/cm
1.0	-0.01	-0.12	-0.28
3.1	-0.01	-0.12	-0.28
5.1	-0.01	-0.13	-0.26

TABLE S2. Temperature coefficients for three pressures of propylene. Typical error associated with these measurements is  $\pm 0.01$  Hz/K for the 0.0 mG/cm and 5.3 mG/cm systems, and 0.03 Hz/K for the 26.5 mG/cm system.

**3.3. Temperature coefficients of gas mixtures.** As mentioned earlier in Section 2.2, mixture composition enters through the viscosity, which is an average of the two gas mixtures. When the ratio of components is altered, the viscosity shifts toward one or the other. In this section, we show that the effect on the temperature calibration coefficient is small. In practice, if one uses the same NMR resonance and molecular species as the NMR signal to yield thermal maps, the calibration coefficient does not change appreciably across mixture composition.

Consider a mixture of propylene and ethane (Table S3). As demonstrated in Table S2, the linewidth exhibits negligible temperature dependence in the absence of an external gradient. For propylene and ethane  $^1\text{H}$  resonances, these linewidths were approximately 14 Hz and 3 Hz, respectively. With the application of an external field gradient, the temperature dependence of linewidth is independent of the component ratio (within experimental error), as seen in Tables S3 and S2.

Additionally, the temperature coefficients of propylene and ethane gases are identical within experimental error. As gradient strength increases, the linewidth becomes increasingly dependent on temperature, as expected. These results suggest that the temperature coefficient may exhibit considerable independence from gas type and mixture composition. The error bars were derived from repeated measurements on different sample preparations and are likely due to differences in shimming.

**3.4. Temperature coefficients in heterogeneous media.** In order to investigate the possibility of dependence on the reactor composition, we have investigated several different reactor types in addition to the glass wool reactors used in the Letter. Packed-bed reactors containing the following catalysts were constructed: silica gel, ZIF-8 (Basolite), and Pd-MOF (Table S4 and Figure S12). In all cases, the reactors were packed with pure catalyst and no glass wool. This type of reactor mimics conditions which are found in a variety of processes. The reactors are shown in Figure S12.

As each of the calibrations correspond to different experiments, initial shims, and therefore, initial linewidths, were quite varied among the three systems. However, the effect of applied magnetic field gradient becomes clear when the linewidths are sufficiently broadened to overwhelm the heterogeneous nature of the packed bed systems. In Table S4 we show the results in the case of strong applied gradients (25.6 and 52.0 mG/cm). As can be seen, the temperature coefficient is independent of the reactor type within experimental error.



Temperature coefficient (Hz/K) at different applied gradient strengths			
propylene/ethane (2/3) mixture			
Gas	0.0 mG/cm	5.3 mG/cm	10.6 mG/cm
Propylene	0.00	-0.15	-0.16
Ethane	0.01	-0.14	-0.16
propylene/ethane (1/14) mixture			
Gas	0.0 mG/cm	5.3 mG/cm	10.6 mG/cm
Propylene	0.00	-0.13	-0.18
Ethane	-0.01	-0.13	-0.15

TABLE S3. Temperature coefficients for propylene/ethane mixtures. Typical error associated with these measurements is  $\pm 0.01$  Hz/K for the 0.0 mG/cm and 5.3 mG/cm systems and  $\pm 0.02$  Hz/K for the 10.6 mG/cm system. Ratios given (2/3 and 1/14) are ratios of gas pressures. Total pressure of the mixtures in each tube was 2.0 atm.

The errors are consistent with differences in shimming, which are additive to the external gradient.

Temperature coefficient (Hz/K) at different applied gradient strengths			
Media	0.0 mG/cm	26.5 mG/cm	53.0 mG/cm
Silica Gel	-0.01	-0.31	-0.92
ZIF-8 (Basolite)	-0.03	-0.29	-0.86
Pd-MOF	-0.01	-0.26	-0.84

TABLE S4. Temperature coefficients for various types of packed-bed catalytic reactors. The typical error bar associated with these measurements on heterogeneous media is  $\pm 0.01$  Hz/K,  $\pm 0.03$  Hz/K and  $\pm 0.09$  Hz/K for the 0.0 mG/cm, 26.5 mG/cm, and 53.0 mG/cm systems, respectively. Pressures of each system were approximately 2.7 atm.

### 3.5. Origin of the inhomogeneous lineshape in heterogeneous media.

3.5.1. *Inhomogeneity effects on temperature coefficient.* Equations (1) and (2) in the main text give temperature coefficients of -0.16 Hz/K and -0.10 Hz/K ( $\pm 0.01$  Hz/K) for the PtNP and Pd-MOF systems, respectively. These values differ from one another by at least 26% using the edges of the error bars. The spin-spin relaxation time,  $T_2$ , of pure propylene was measured to be  $(68 \pm 11)$  ms using a Carr-Purcell-Meiboom-Gill (CPMG) echo train sequence of 100 echoes with an echo spacing  $\tau = 10$  ms. The final observed linewidth in the presence of the external gradient was approximately 90 Hz. Of this, 5 Hz are due to contributions from  $T_2$ , which is essentially temperature independent over the range studied. This leaves

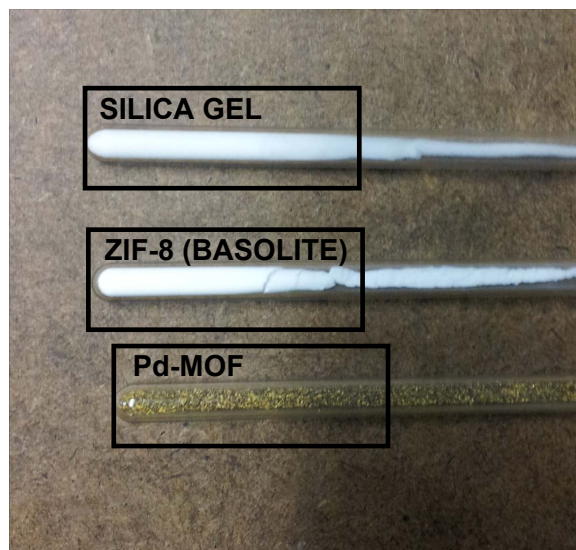


FIGURE S12. Packed bed reactors containing silica gel, ZIF-8, and Pd-MOF. The RF region of each reactor is boxed.

about 85 Hz caused by field gradients, which will give rise to temperature-dependent effects. The gradients are the sum of the applied (external) gradient and shims.

In the absence of an applied gradient ( $G_T$ ) the NMR linewidth averaged over the entire PtNP reactor volume was 41 Hz for this particular reactor. Under the same conditions, the average NMR linewidth over the entire Pd-MOF system was 31 Hz. The contribution from residual field inhomogeneities,  $(\pi T_2^\dagger)^{-1}$ , can be estimated from knowledge of  $T_2$  and the measured linewidth in the absence of a gradient,  $(\pi T_2^*)^{-1}$  using Eq. (26),

$$(26) \quad \frac{1}{\pi T_2^*} [Hz] = \frac{1}{\pi T_2} [Hz] + \frac{1}{\pi T_2^\dagger} [Hz].$$

This yields  $(\pi T_2^\dagger)^{-1} = 36$  Hz and 26 Hz for the PtNP and Pd-MOF systems, respectively. These figures represent a substantial fraction (nearly one-third to one-half) of the 85 Hz contribution to the linewidth from all field inhomogeneities. Thus, differences in residual shim can likely explain the differences in observed temperature calibration coefficients. A more exact comparison is not available due to the substantial complications associated with measuring  $T_2$  in a gas and the lack of knowledge of the exact nature of the residual shims (spatial pattern and direction).

**3.5.2. Linewidth over a single voxel.** For the method to yield measurements that are independent of the reactor medium, it is important that the external gradient overwhelms the linewidth in the region of interest. Thus, it is instructive to examine the line broadening effect from the external gradient and compare it to the local linewidth in the absence of a gradient. We have seen in the Letter that the linewidth over the entire reactor was broadened by a factor of five (5) or greater. At the level of a single voxel, the external gradient must overwhelm the linewidth as well.

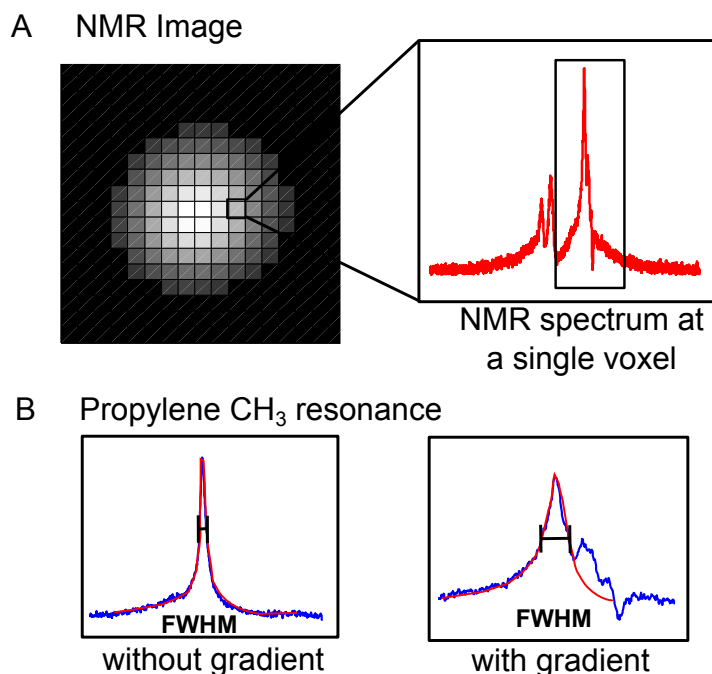


FIGURE S13. (a) Spectroscopic imaging produces a gas density image of the PtNP reactor system, in which each voxel contains its own NMR spectrum. Voxel size is approximately  $0.7 \times 0.7 \text{ mm}^2$ . (b) At each voxel, linewidth  $\Delta f$  is determined by the full width at half maximum (FWHM) of a resonance. In the presence of applied magnetic field gradient  $G_T$ , the FWHM of the methyl resonance is broadened by a factor of 5. Here we compare the linewidth prior to reaction and without gradient  $G_T$  to the linewidth during a reaction with an applied gradient  $G_T$ .

The local linewidth can be mapped with an MRI experiment by using spatial encoding, with and without the “temperature-encoding gradient,”  $G_T$ . Figure S13 depicts an axial view of the PtNP reactor’s propylene density. When the NMR experiment is performed on the reactor, without the gradient  $G_T$ , propylene’s methyl resonance yields a voxel linewidth  $\Delta f$  of 17 Hz. However, when the NMR experiment is performed during a catalytic reaction, and with the applied gradient  $G_T$ , the linewidth broadens significantly within a voxel. As shown in Figure S13(b), the propylene and propane resonances overlap, so it is necessary to fit the data to a sum of Lorentzians. Doing this yields broadened resonances with linewidths up to 90 Hz as compared to 17 Hz without the gradient. Thus, the gradient-induced line broadening at the single-voxel level is approximately five-fold. The line broadening over a single voxel is nearly identical to that over the entire reactor volume.

**3.5.3. Lineshape over a single voxel.** In the general case, the voxel lineshape depends on the magnitude of the temperature gradients contained within a voxel. For exceedingly large gradients the signal is best described by a stretched exponential (Kohlrausch) function, which

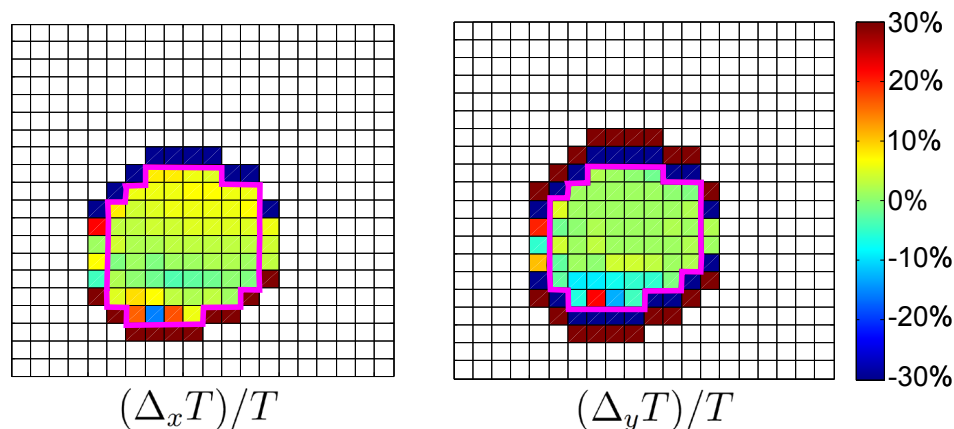


FIGURE S14. Maps of the finite differences in temperatures between nearest-neighbor points relative to the local temperature:  $(\Delta_x T)/T$  and  $(\Delta_y T)/T$ . These maps represent the differences in temperature between neighboring voxels (along  $x$  or  $y$ ). For temperature profiles which are monotonic across a voxel, this finite difference provides an “upper bound” for the magnitude of the temperature gradient within a voxel. As can be seen, these internal gradients over a voxel are fairly small on average ( $< 4\%$ ). Points near or at the edges are unphysical due to the large derivatives at the boundaries.

models sums of exponentials. The effective linewidth is the weighted mean of the individual contributing linewidths, and the “width” of the distribution is encoded in the stretched exponent [11].

In our experiments, however, these gradients are quite small on the absolute temperature scale. The maximum “fractional” temperature change from voxel to voxel was found to be less than 4% on average, as shown in Figure S14. Furthermore, all spectral data were well described by Lorentzian lines, which is further evidence that the temperature gradients within voxels are not a problem.

**3.5.4. Thermal flux and catalyst packing.** In a catalytic reactor the transport of heat is of prime importance. The dynamic quantity of interest is the flux of energy (e.g. internal energy or enthalpy of the system), which is proportional to the local temperature gradient  $\|\nabla T\|$ . The temperature gradient can be estimated numerically from the thermal maps using finite differences (Figure S15). When compared to a  $\mu$ -CT scan of the microreactor, we notice that the length scales of energy flux are similar to those of the glass wool/catalyst packing. The  $\mu$ -CT images shown below are of a typical PtNP reactor packed with glass wool. The CT scan represents a 1 mm-thick slice through the middle of the reactor, whereas the MRI images (Figure 3) are projections along the thickness of the reactor. We note that, although the reactor construction process is identical, the reactor shown in the  $\mu$ -CT image is not necessarily the same reactor as that shown in the MRI image and the images are not co-registered. Our statement only refers to the typical length scales found in such reactors.

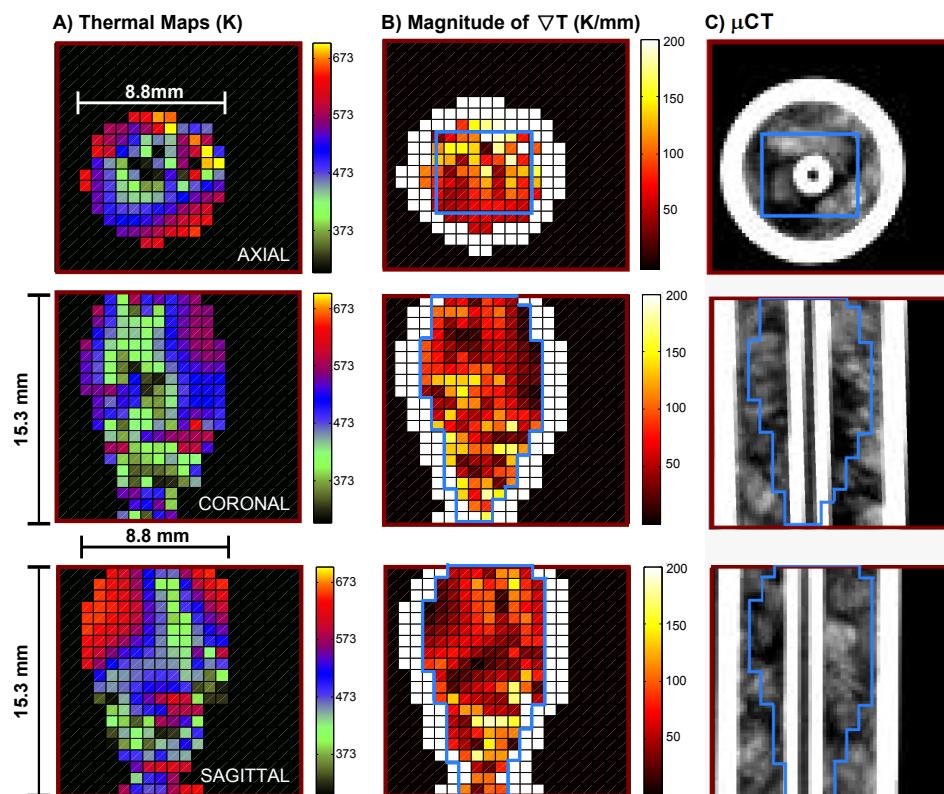


FIGURE S15. Typical length scales in a PtNP reactor system. (a) Thermal maps of the PtNP reactor system. (b) Magnitude of  $\nabla T$ , the numerical gradient of temperature across the PtNP reactor. (c)  $\mu$ -CT images of NMR reactor.

## 4. REFERENCES

- (1) Bloembergen, N., Purcell, E.M., Pound, R.V. (1948) Relaxation Effects in Nuclear Magnetic Resonance Absorption, *Phys. Rev.*, 73(1):679-712
- (2) Kubo, R., Tomita, K. (1954) A General Theory of Magnetic Resonance Absorption, *J. Phys. Soc. Japan*, 9:888
- (3) Kubo, R. (2007) A Stochastic Theory of Line Shape, in *Advances in Chemical Physics: Stochastic Processes in Chemical Physics*, Volume 15 (ed K. E. Shuler), John Wiley & Sons, Inc., Hoboken, NJ, USA. doi: 10.1002/9780470143605.ch6
- (4) Huang, R., Chavez, I., Taute, K.M., Lukić, B., Jeney, S., Raizen, M.G., Florin, E.-L. (2011) Direct observation of the full transition from ballistic to diffusive Brownian motion in a liquid, *Nat. Phys.*, 7:576-580
- (5) Nørrelykke, S.F., Flyvbjerg, H. (2011) Harmonic oscillator in heat bath: Exact simulations of time-lapse-recorded data and exact analytical benchmark statistics, *Phys. Rev. E*, 83:041103
- (6) Bromley, L.A., Wilke, C.R. (1951) Viscosity behavior of gases, *Industr. Eng. Chem.*, 43(7):1641-1648
- (7) Whitaker, S. (1986) Local thermal equilibrium: an application to packed bed reactor design, *Chem. Eng. Sci.*, 41(8):2029-2039
- (8) Torquato, S. (2001) *Random heterogeneous materials: from microstructure to macroscopic properties* (Springer, New York)
- (9) Whitaker, S. (1999) *The method of volume averaging* (Springer, New York)
- (10) Quintard, M., Whitaker, S. (1993) Transport in ordered and disordered porous media: Volume-averaged equations, closure problems, and comparison with experiment, *Chem. Eng. Sci.*, 48(14):2537-2564
- (11) Johnston, D.C. (2006) Stretched exponential relaxation arising from a continuous sum of exponential decays, *Phys. Rev. B*, 74(18):184430.